

Marmousi2: An elastic upgrade for Marmousi

GARY S. MARTIN, GX Technology, Houston, USA

ROBERT WILEY and KURT J. MARFURT, University of Houston, USA

The original Marmousi model was created by a consortium led by the Institut Français du Pétrole (IFP) in 1988. Since its creation, the model and its acoustic finite-difference synthetic data have been used by hundreds of researchers throughout the world for a multitude of geophysical purposes, and to this day remains one of the most published geophysical data sets. The advancement in computer hardware capabilities since the late 1980s has made it possible to perform a major upgrade to the model and data set, thereby extending the usefulness of the model for, hopefully, some time to come. This paper outlines the creation of an updated and upgraded Marmousi model and data set which we have named Marmousi2.

We based the new model on the original Marmousi structure, but extended it in width and depth, and made it fully elastic. We generated high-frequency, high-fidelity, elastic, finite-difference synthetics using a state-of-the-art modeling code made available by Lawrence Livermore National Laboratory as part of a U.S. Department of Energy research project. We simulated streamer, OBC, and VSP multicomponent shot records with offsets up to 15 km.

We have found these data suitable for a wide variety of geophysical research including calibration of velocity analysis, seismic migration, AVO analysis, impedance inversion, multiple attenuation, and multicomponent imaging. As part of this project, the Marmousi2 model and data set are available to other researchers throughout the world.

The Marmousi2 structural model. We created the Marmousi2 model by first reconstructing the original Marmousi model. The original Sierra Geophysical format horizon files have been lost with the passage of time, so we needed to

Table 1. Seismic resolution for different depths in the model and varying dominant frequency

f (Hz)	Shallow (V=1800 m/s)		Middle (V=3000 m/s)		Deep (V=4000 m/s)	
	λ (m)	$\lambda /4$ (m)	λ (m)	$\lambda /4$ (m)	λ (m)	$\lambda /4$ (m)
20	90.00	22.50	150.00	37.50	200.00	50.00
30	60.00	15.00	100.00	25.00	133.33	33.33
40	45.00	11.25	75.00	18.75	100.00	25.00
50	36.00	9.00	60.00	15.00	80.00	20.00

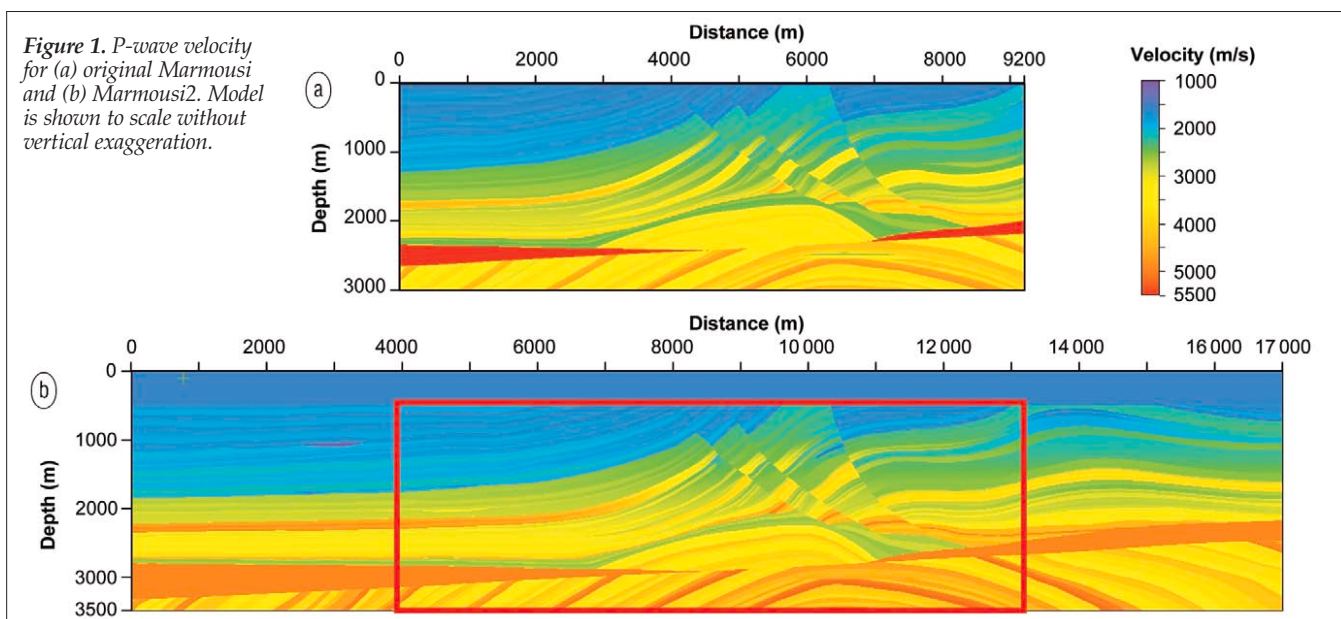
recreate the horizon segments from the gridded representations of the model provided to us by colleagues at IFP.

Once these horizons were regenerated, we expanded the model from 9.2 km to 17 km in width and from 3 km to 3.5 km in depth to better simulate long-offset acquisition in a deepwater setting (Figure 1). The original Marmousi model is close to the center of Marmousi2. We extended the horizons in the original model to fit the expanded model and added 41 new horizons, bringing the total number of horizons in Marmousi2 to 199. Since we are interested in evaluating amplitude preservation for AVO analysis, the augmented Marmousi2 model now includes several additional structurally simple, but stratigraphically complex features outside the original zone of complex structure (Figure 2). We also inserted several reservoirs to explicitly model channels and other hydrocarbon traps in both the original and new part of the Marmousi2 model.

Since deepwater exploration (including OBC acquisition) is now of significant interest, we replaced the previous ~32-m water layer with a 450-m water layer. For the same reasons, the original "hard water bottom" effect was reduced by adding two flat transitional layers with thicknesses of 25 m and 30 m above the original water bottom. As a result, the original Marmousi structures are approximately 473 m deeper in Marmousi2.

We did not change layer thicknesses from the original

Figure 1. P-wave velocity for (a) original Marmousi and (b) Marmousi2. Model is shown to scale without vertical exaggeration.



model. Typically the sediment layers have a thickness in the range of 20–100 m, although minimum thickness ultimately approaches zero at pinchouts and truncations.

Seismic resolution is defined in terms of seismic wavelength, $\lambda = V/f$, where λ is the seismic wavelength, V is the velocity, and f is the dominant frequency. The resolvable limit is normally expressed as $\lambda/4$.

Example values of seismic resolution and the corresponding resolvable limit for representative shallow, middle depth, and deeper parts of the model are shown in Table 1. A range of dominant frequencies, compatible with typical surface seismic data and the actual modeling wavelet, is used for illustration. The wavelet itself is discussed in detail in a later section, and is shown in Figure 8.

Table 1 shows that while some formations will be individually resolved, the majority of reflection events will be composites consisting of the interference of more than one formation in our earth model. Thus, although our 199 horizons define formations that are coarser than in the real earth, the resulting events will mostly be composites.

Layer properties. The original Marmousi model was an acoustic model—i.e., it only supported the propagation of compressional (P-) waves. Marmousi2 is a fully elastic model that supports not only compressional waves, but also shear waves, converted waves, and all manner of guided waves including those traveling along the sea floor. To define this model we needed to assign a shear velocity as well as the original compressional velocity and density to each layer.

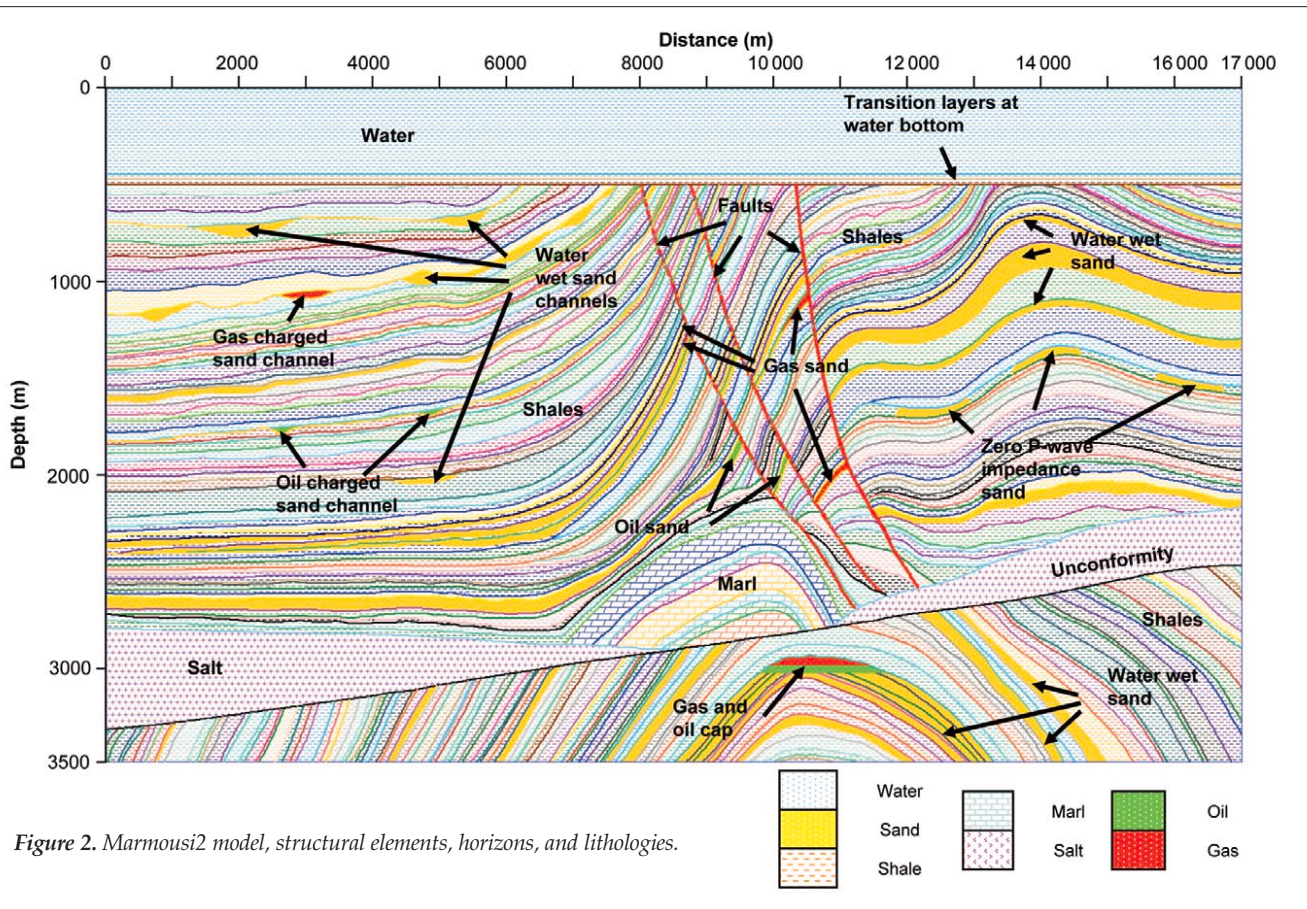
In order to assign reasonable shear veloc-

ities, lithologies were first assigned to each layer. The Marmousi model was based upon geology from the North Quenguela Trough in the Quanza Basin of Angola, and although the lithologies were not assigned in the model (except for salt and water), the lithologies were described (Versteeg, 1994). The section is primarily composed of shale units, with occasional sand layers. The core of the complex faulted area is an anticline that is composed of marl. An unconformity and a partially evacuated salt layer separate the marls from the deeper anticlinal units, which are also mostly shales with some sand.

We assigned lithology to Marmousi2 (Figure 2) using the following policies. The salt and water layers from the original model are preserved. The first two layers (transitional layers) are shale, and possess properties consistent with soft modern sediments. All layers containing hydrocarbons must be sand. The anticline above the salt is composed of marl—i.e., carbonate rich shales. All other layers are either sand or

Table 2. Velocities and density for the lithologies

	V_P (m/s)	V_S (m/s)	ρ (g/cm ³)
Water	1500	0	1.01
Sand	From Marmousi	$V_S = 0.804V_P - 856$	$\rho = 0.2736V_P^{261}$
Shale	From Marmousi	$V_S = 0.770V_P - 867$	$\rho = 0.2806V_P^{265}$
Salt	4500	2600	2.14
Limestone	From Marmousi	$V_S = 1.017V_P - 0.055V_P^2 - 1030$	$\rho = 0.3170V_P^{225}$



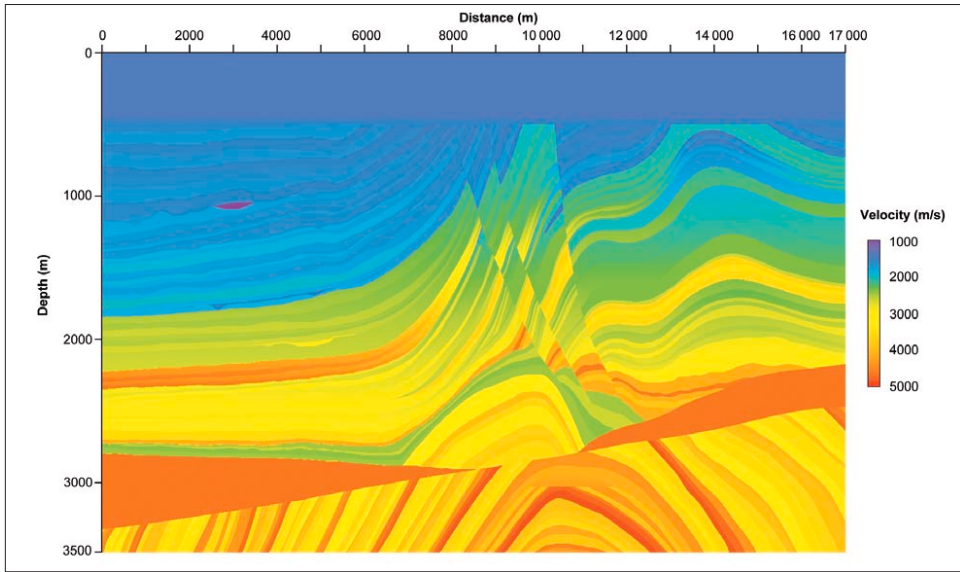


Figure 3. Marmousi2 P-wave velocity.

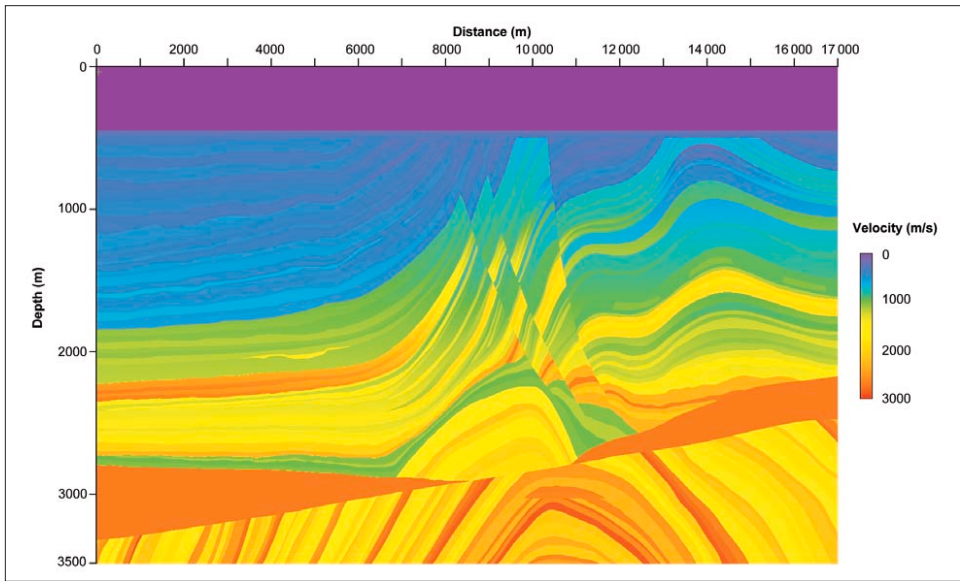


Figure 4. Marmousi2 S-wave velocity.

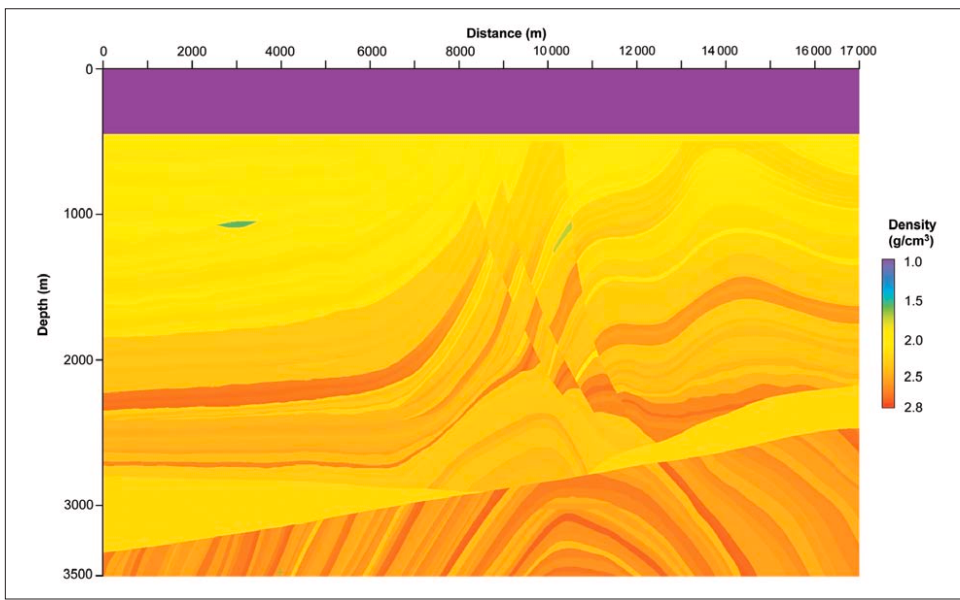


Figure 5. Marmousi2 density.

shale, with the majority of layers being shale. The sand layers were picked out by analyzing the density of the original model assuming that sands are typically less dense than shale.

Regardless of the designated lithology, the layers were initially given a P-wave velocity identical to the original Marmousi model. We defined the P-wave velocity using either a constant velocity or a simple compaction model of $V = V_0 + kz$, where z is depth below sea level, k is a "compaction gradient" term, and V_0 is the velocity intercept at datum. Since velocity gradients account for compaction due to overburden loading (and thus water depth is irrelevant), we adjusted the velocity definitions accordingly using the following equation: $V_{0\text{new}} = V_0 \text{old} - (k * 468)$ where 468 is the repositioned average depth of the original waterbottom in meters. Thus, the gradients (k) are unchanged, but the intercepts at datum (V_0 values) are reduced. The new layers were assigned P-wave velocities similar to the neighboring units. We display our final P-wave velocity model in Figure 3.

Given the lithology and the P-wave velocity, we applied the Greenburg and Castagna (1992) transforms to obtain the S-wave velocity (Figure 4), and the Castagna et al. (1993) transforms for obtaining the density (Figure 5). We reproduce these transforms (which are defined for water-wet sediments) in Table 2, which also shows the values for the other lithologies in the model.

The P-wave velocity of the salt layer was reduced significantly from the value in the original model (5,500 m/s). We reduced the value to 4,500 m/s, which is a more commonly used velocity for salt. Correspondence with velocity modeling experts at Elf Aquitaine working in Angola confirmed that the previous figure was probably too fast.

We calculated the properties for the marl units using the equations given above for shale and limestone. Using the Voight-Reuss-Hill method (related by Hilterman, 2001), we described the marls as 70% shale and 30% limestone.

Table 3. Dimensions of hydrocarbon layers *

ID	Index	Feature length (m)	Average vertical thickness (m)	Average thickness (m)	Hydrocarbon content
A	013_GAS	780	38	38	Gas
B	033_OIL	2940	40	40	Oil
C1	049_GAS	135	26	22	Gas
C2	051_GAS	133	55	45	Gas
C3	053_GAS	435	53	45	Gas
C4	071_GAS	340	75	60	Gas
D1	071_OIL	255	75	45	Oil
D2	071_OIL	540	49	38	Oil
E1	177_GAS	1395	50	50	Gas
E2	178_OIL	1890	42	42	Oil

*Layer IDs are shown in Figure 6.

Hydrocarbons. Since one of our primary goals was to provide a realistic model to evaluate the impact of prestack depth imaging on AVO, we introduced a series of hydrocarbon layers into the structural model. We display these hydrocarbons as red (gas) and green (oil) in Figures 2 and 6. The hydrocarbons are distributed within the complex faulted zone at different depths, and also in the simple structure on the flanks. These layers vary in their size, shape, structural complexity, and hydrocarbon content (Table 3).

We introduced gas and varying GOR oil using standard fluid substitution techniques. In order to simplify the fluid substitution calculations, we assigned each hydrocarbon-bearing layer a single value for P-wave velocity by calculating the value at the average depth of the unit. Furthermore, we assumed

that all hydrocarbon layers are normally pressured, at a temperature of 95°C, with a mudweight of 10 lb/gallon, a water saturation of 30%, and an API of 30. The gas/oil ratio is expressed in cubic feet of gas per barrel at the surface (used/maximum).

In Table 4 we show the results of our fluid substitution. Hydrocarbon substitution results in a drop of the P-wave velocity, a minor increase of the S-wave velocity, and a small decrease of the density. The V_p/V_s ratio and acoustic impedance values both decrease after fluid substitution.

Table 4. Fluid substitution results *

ID	Fluid	Gas-oil ratio	Thickness (m)	Depth (m)	Water-wet sand			Hydrocarbon-charged sand		
					V_p (ms)	V_s (m/s)	ρ (g/cc)	V_p (ms)	V_s (m/s)	ρ (g/cc)
A	GAS	-	38	1080	1753	553	1.92	1028	607	1.59
B	OIL	250/609	40	1700	1855	635	1.94	1640	652	1.85
C1	GAS	-	26	1250	2210	921	2.04	1770	988	1.77
C2	GAS	-	55	1300	2480	1138	2.10	2131	1209	1.86
C3	GAS	-	53	1150	2080	816	2.00	1584	881	1.72
C4	GAS	-	75	1900	3025	1576	2.21	2783	1645	2.03
D1	OIL	270/686	75	1900	3025	1576	2.21	2874	1604	2.14
D2	OIL	270/686	49	1900	3025	1576	2.21	2874	1604	2.14
E1	GAS	-	50	3000	4200	2521	2.44	4045	2564	2.36
E2	OIL	300/1100	42	3050	4200	2521	2.44	4123	2538	2.41

*Layer IDs are shown in Figure 6.

Comparison of the fluid substitution results for the anticlinal hydrocarbons and the original Marmousi model illustrates that the original model possessed incredibly large changes in velocity and density that cannot be supported by fluid substitution. We assume that these somewhat extreme values were emplaced into the model to ensure a very strong reflectivity response for these units.

Other model features. We also introduced several sand units that should not be detectable by P-wave data alone.

The units have P-wave and density values identical to the surrounding layers so that there is no P-wave impedance change. The shear-wave values were modified from the values given by the transforms in order to exhibit a small shear wave impedance change.

Synthetic data generation. The major acquisition objectives for Marmousi2 were to create a high quality, multicomponent, high-frequency, elastic synthetic data set over a complex structural model. In order for synthetic seismic data to be useful for calibrating data-processing algorithms, the modeling process must accurately emulate the physical experiment. At the very least, the forward modeling methods must be more accurate than the inverse methods that will be tested.

The elastic wave equations describe the propagation of both compressional and shear waves, and implicitly handle mode conversions. Forward modeling with the elastic wave equations should therefore provide data with many of the events seen in real data, including primaries, multiples, diffractions, converted waves, head waves, surface waves, interface waves, and complex scattering. By using an elastic model we will be able to better evaluate multicomponent processing workflows, the impact of converted waves on P-wave velocity analysis and imaging, multiple suppression in the presence of S-waves and converted waves, and AVO.

For reasons of computational cost, we did not include 3D effects, and for reasons of simplicity, we did not include anisotropy and attenuation. Since one of our goals is to provide the horizons and layer parameter models to other researchers, who may wish to generate subsequent (and more complex) versions of this model for internal or public use, we encourage others to embrace this task and share their results.

Geometry. We acquired a full set of elastic shot records over the model. We show the spacing of the sources and receivers in Table 5 and Figure 7.

The source is a synthetic air gun with a firing depth of 10 m. The sailing direction for the source vessel is from low values of X (left) to high values of X (right).

The source signature is a zero-phase 5-10-60-80 Hz Ormsby wavelet with frequencies up to 80 Hz (Figure 8). The computation of 2D models typically involves the use of a “line source” due to the limitations of 2D modeling. A line source differs considerably from a “point source” in that it has

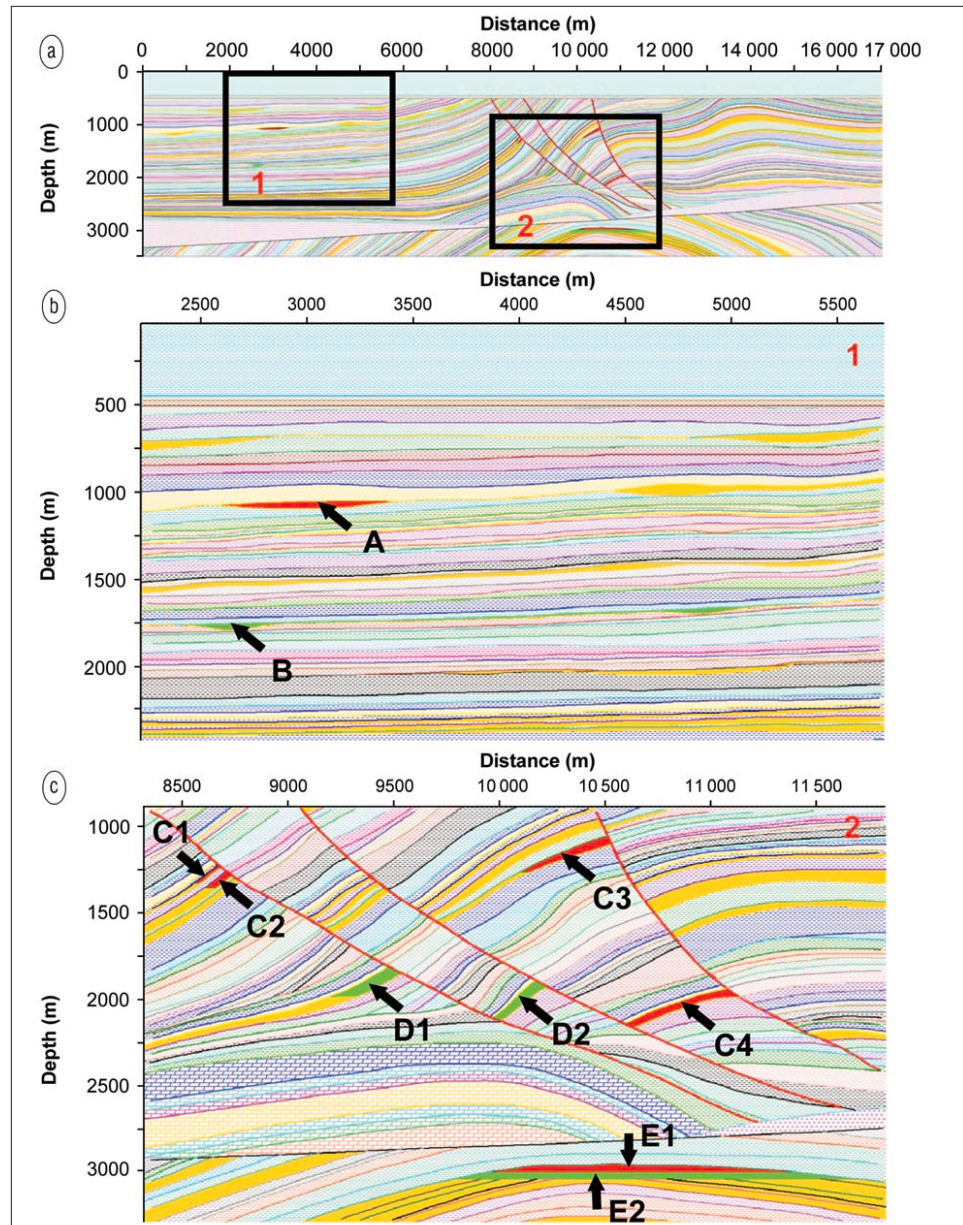


Figure 6. Hydrocarbon units. (a) Overview shows location of hydrocarbon units and areas shown in greater detail in (b) and (c). (b) Location of hydrocarbon units in a relatively simple structural setting. (c) Location of hydrocarbon units in more structurally complex locations.

$1/R^{1/2}$ rather than $1/R$ amplitude decay. Also, it has increased low-frequency content proportional to $1/f^{1/2}$, and most important, it has a phase rotation of 45° . To better approximate the phase and frequency content of 3D propagation, we modify our 2D finite difference source by applying a 45° phase rotation, time shift, and frequency filter to provide a far-field, zero-phase wavelet, consistent with one we would obtain if we could afford to model the data in 3D (Figure 8).

The data were recorded using receivers located along two horizontal lines (the streamer depth at 5 m below sea level and the OBC measurement depth at the water bottom of 450 m below sea level), and one vertical location (the VSP). The “streamer” cable recorded a hydrophone response (pressure) at 1361 locations with a group interval of 12.5 m, representing a currently unrealistic 17-km cable. For simplicity, and to allow workers the ability to process data with alternative acquisition programs such as two ship experiments, the cable also extended all 17 km across the model (including

in front of the “boat”). The “OBC” cable recorded pressure, the vertical component of particle velocity (V_z), and the horizontal component of particle velocity (V_x), using a hydrophone and two orthogonal geophones respectively. The OBC cable was fixed at the water bottom and had 1381 locations and a group interval of 12.32 m. The unusual grouping distance resulted from parameterization difficulties within the modeling software. The vertical “VSP” cable recorded both hydrophone and two-component geophone responses. In addition, a theoretical “shear phone” was used. Shear phones do not exist in the real world but can be simulated in the modeling software, recording a wavefield proportional to the shear wave component of the energy. The vertical cable was at $X=10\ 300$ m, with receivers from the free surface to bottom of the model. Receiver groups were spaced every 12.5 m in depth, making a total of 281 receiver groups. Every receiver was “live” (recorded data) for every shot, so, the offset distribution of the data has not been limited to standard streamer lengths or geometries.

Model boundaries. The data were acquired with a reflecting free surface, which simulates an air/water interface. The reflecting free surface is commonly the most significant source of multiples in marine data. The remaining boundaries are absorbing, such that most energy passing out of the model does not reflect back into the model. The modeling software employs a variation of the Clayton Engquist (1990) boundary conditions.

Calculation grid. We chose our calculation grid based on well understood limits of numerical accuracy. Grids that are too coarse result in a faster computation but with both numerical dispersion and numerical anisotropy. The grid sampling is given by

$$\text{grid.sampling} = \frac{\text{min.velocity}}{\text{max.frequency} * \text{samples.per.wavelength}}$$

To avoid numerical dispersion, approximately five samples per wavelength are required for the slowest velocity in the model (Levander, 1988). The slowest velocity is approximately 270 m/s (shear-wave velocity), and the maximum frequency is 80 Hz. Theoretically, using five samples per wavelength, a grid size of 0.42 m is required, but this was impractical for the assigned computational resources. However, looking more closely at the model, it is clear that only a very small portion of the model has velocities with values this low. A more reasonable average minimum shear wave velocity is around 400 m/s. The required grid size becomes 1 m for 80 Hz, 1.14 m for 70 Hz, and 1.33 m for 60 Hz.

Table 5. Source and receiver geometry for Marmousi2 acquisition, see Figure 7

Sources	origin	end	X (m)	inc.	#	Depth	Type			
Towed source	3000	14975	25		480	10m	Airgun			
Streamer & OBC receivers	origin	end	X (m)	inc.	#	Depth	pressure			
Streamer	0	17000	12.5		1361	5	yes			
OBC	0	17000	12.32		1381	450	yes			
VSP receivers	location	X (m)	Z (m)	inc.	#	pressure	Vz	Vx	shear	
VSPs	10300	1	0	3500	12.5	281	yes	yes	yes	yes

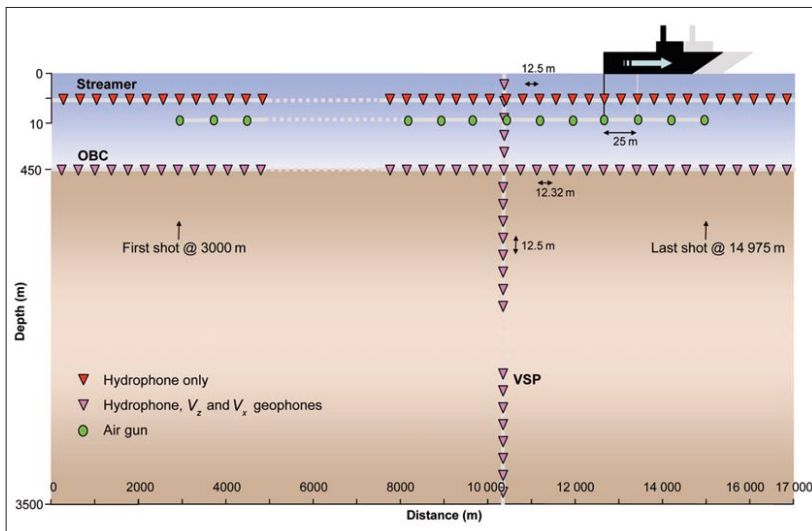


Figure 7. Acquisition geometry for Marmousi2. Diagram is not to scale.

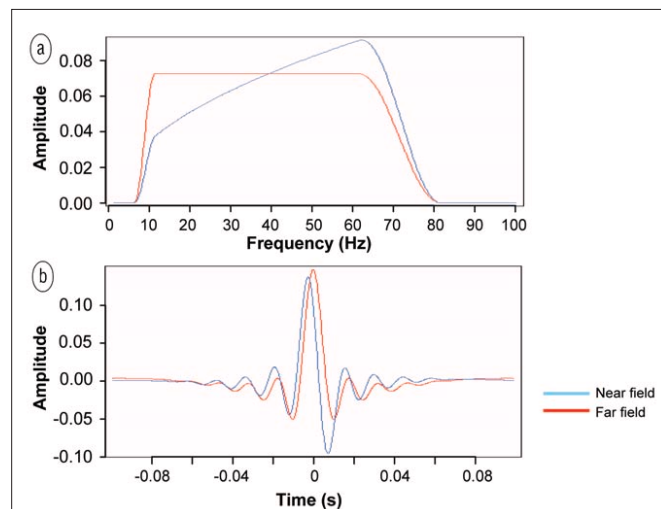


Figure 8. (a) Amplitude spectra and (b) wavelet for the source. The blue line represents the actual modeling source wavelet and also characterizes the signature in the near field. It was derived from the 5-10-60-80 Hz Ormsby wavelet (red line) by applying modifications to provide a far-field signature consistent with a point source rather than a line source. The red line is the initial 5-10-60-80 Hz Ormsby wavelet, and also represents the modeling signature in the far field.

Practical memory and runtime limitations resulted in a compromise. The final grid spacing was 1.25 m. This gives only 2.7 samples per wavelength for the very highest frequency and absolute minimum velocity, which will result in some dispersion of the wavefield, in the thin layer below the water column. Practical folks that we are, we now proclaim our inaccurately modeled isotropic bottom to be a more complex anisotropic dispersive water bottom complex. However, for all velocities over 400 m/s and all frequencies below ~65 Hz, there should be no numerical anisotropy or dispersion.

Computation. The University of Houston provided the computational resources to create the synthetic data, with a mix of funding from the Department of Energy's "Next Generation Modeling and Imaging Project," and Sun Microsystems' UH Geoscience Center of Excellence. Twenty nodes of a Sun 6800 Starfire system were used for a total of five months. We performed finite-difference elastic wave modeling using the E3D modeling code developed at Lawrence Livermore National Laboratory. E3D is second-order accurate in time and fourth-order accurate in space.

The computation time averaged about 20 hours per shot using 6 nodes of the system—i.e., about 4½ CPU days per shot. The data were acquired between September 2002 and January 2003, using a total of 5 CPU months, which is equivalent to 70 000 CPU hours, or approximately 8 CPU years!

Results. We simulated and recorded multicomponent wavefront snapshots, acoustic surface seismic shot records, multicomponent OBC seismic shot records, and multicomponent VSP seismic shot records.

The wavefront snapshots were recorded on a 1.25-m grid covering the entire model. The time interval between snapshots is 100 ms, making a total of 50 snapshots within the time range of 0.1 – 5.0 s. There are two snapshots for each shot, representing P-waves and S-waves. Snapshots were recorded only for every 40th shot, due to their large size and storage requirements. The 14 snapshot locations are spaced evenly every 1000 m, from 3000 to 15 000 m. The snapshot display uses a custom color wheel and blending to combine the P-waves, S-waves, and velocity (Figure 9). Pure P-wave modes appear with a blue-yellow color scale, pure S-wave modes appear with a pink-green color scale, while mixed mode guided and evanescent waves either fall in between or rotate between the two. The Marmousi2 P-wave interval velocity model is mapped to a gray scale image behind the wavefronts. Figure 9 shows a zoomed image of one snapshot ($t=1.4$ s) with certain features labeled.

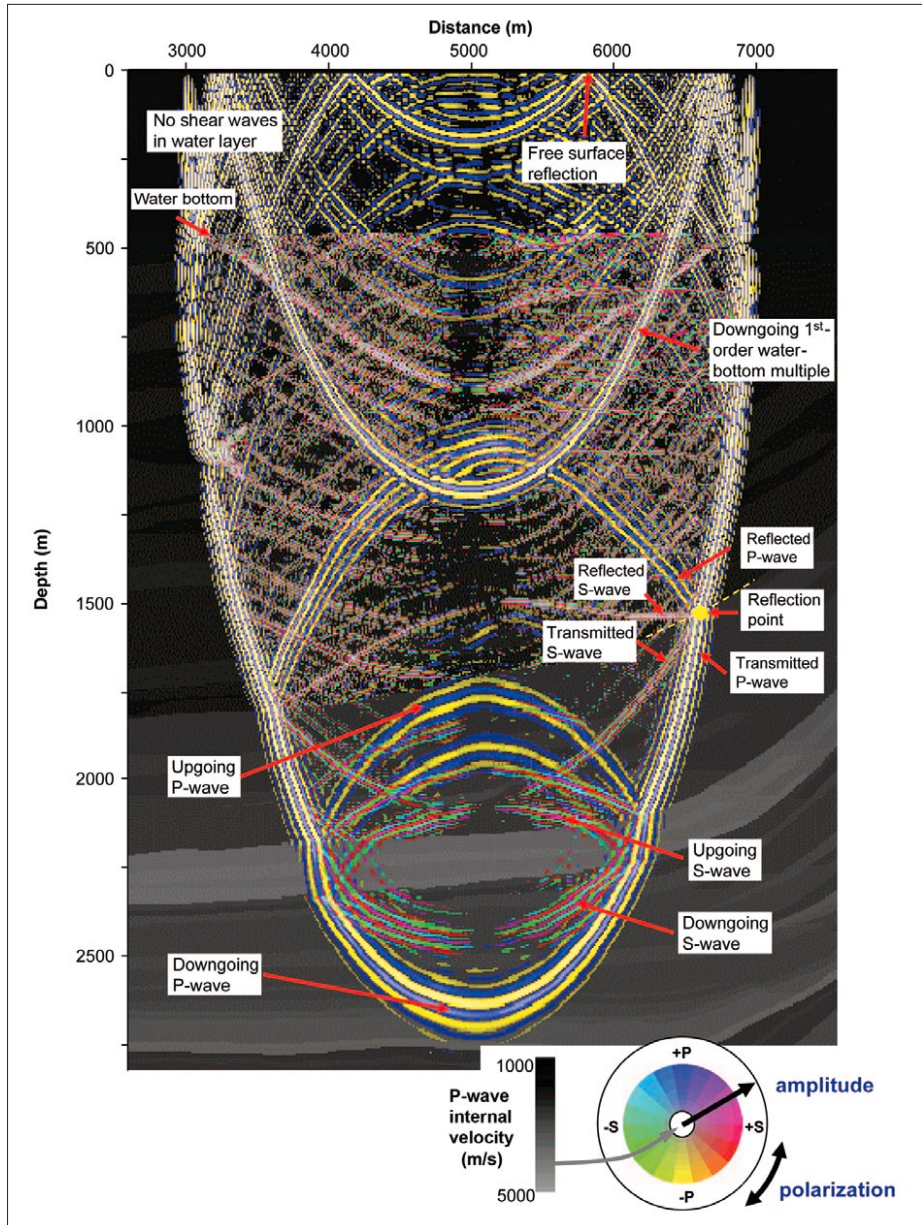


Figure 9. Wavefront snapshot for source 201 (at $X=5000$ m), and $t=1.4$ s. Selected downgoing and upgoing P-waves (blue-yellow) and S-waves (red-green) are labeled. P-wave velocity is shown in the background in gray scale.

The snapshots clearly show that the water bottom is a strong multiple generator. The high-velocity beds reflect a large amount of energy, which reduces energy propagating to the deeper parts of the model. There is also an abundance of mode conversion taking place within the subsurface. The stronger (higher acoustic impedance) events tend to be the source for much of the mode conversion.

The shot records were recorded with a time sampling of 2 ms and a record length of 5 s. Figure 10 shows the surface seismic shot record for shot 285 ($X=7100$ m). Figures 11-13 show the OBC shot records, also for shot 285. Certain features are identified and labeled in the figures. The shot records closely resemble real field shot records, both in terms of the number of events and complexity. The elastic modeling has appeared to create very realistic data from the synthetic model.

The single vertical cable, at $X=10\ 300$ m, recorded data for every shot. Therefore there are 480 records for each of the hydrophone, V_Z geophone, V_X geophone, and shear-

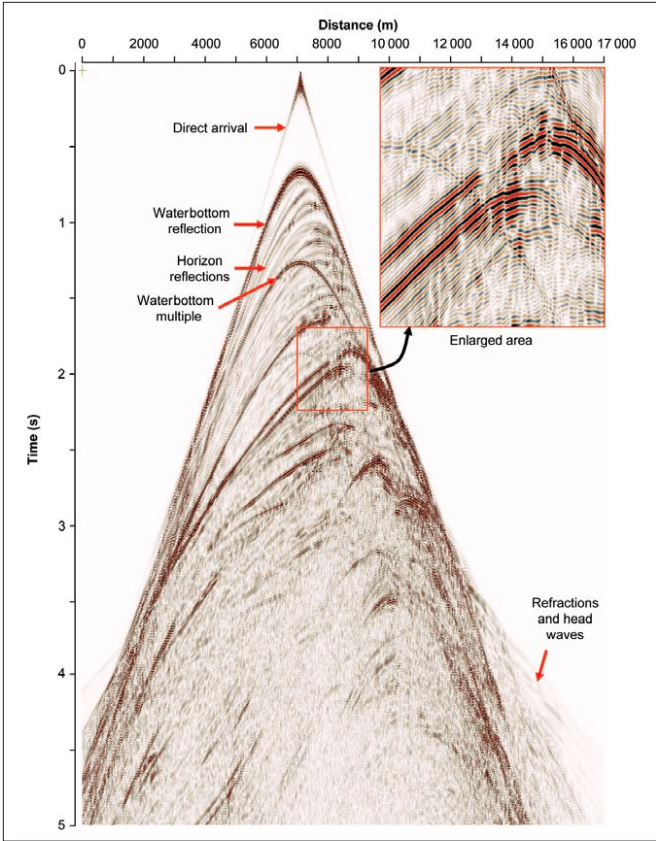


Figure 10. Streamer pressure, shot record 285 ($X=7100\text{ m}$).

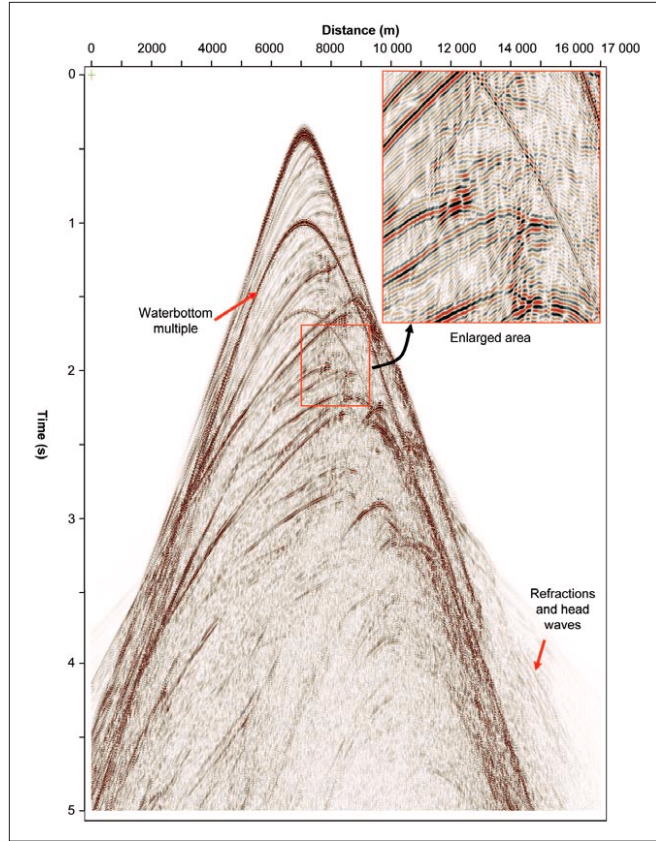


Figure 11. OBC pressure, shot record 285 ($X=7100\text{ m}$).

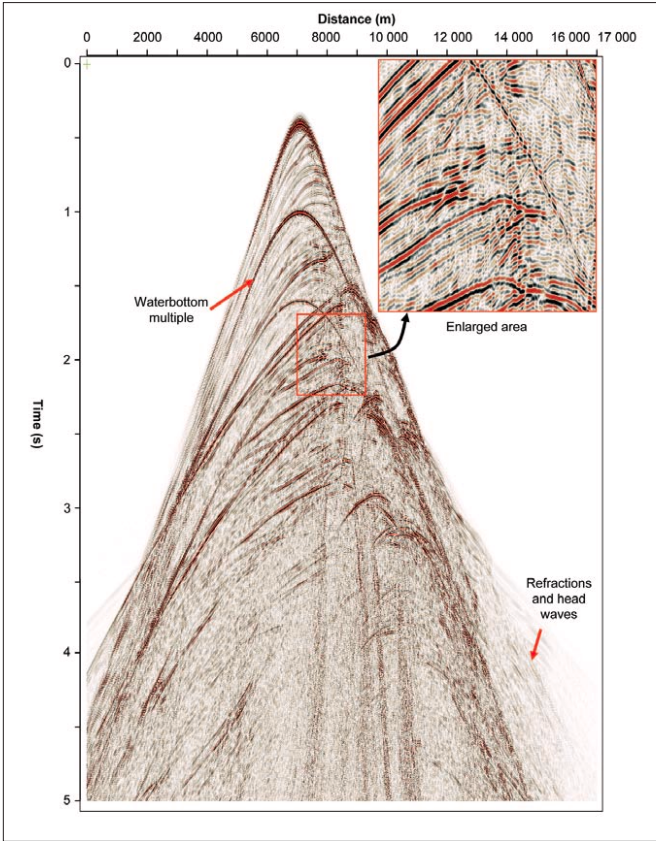


Figure 12. OBC vertical velocity, shot record 285 ($X=7100\text{ m}$).

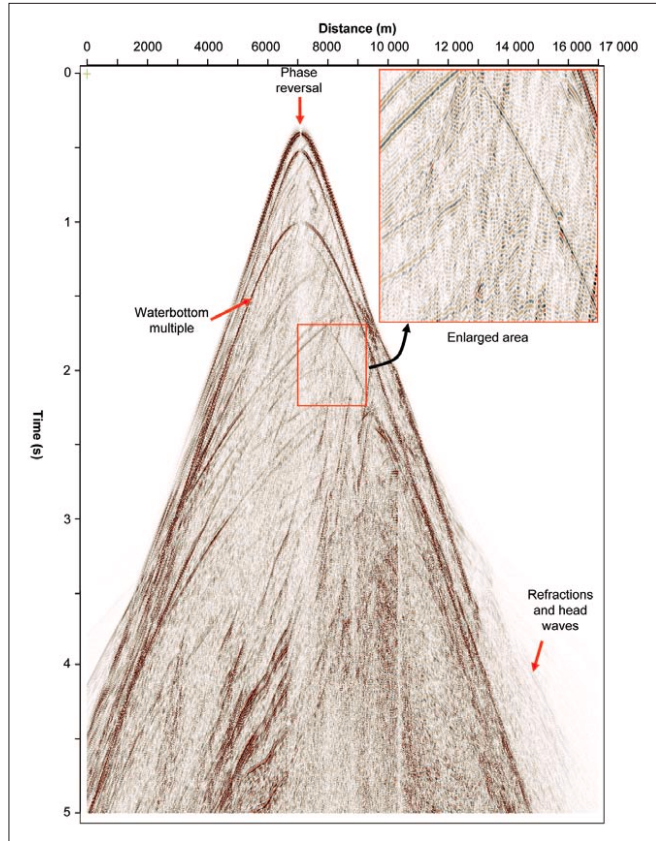


Figure 13. OBC horizontal velocity, shot record 285 ($X=7100\text{ m}$).

phone receivers. A suite of VSP records for a near-offset location (shot 412, $X=10\ 275\text{ m}$, source-to-receiver offset of 25 m) is shown in Figure 14. The near offset VSP records show that energy propagating into the earth is dominantly P-

wave energy, but that considerable mode conversion is taking place.

Conclusion. We have created an updated 2D fully elastic

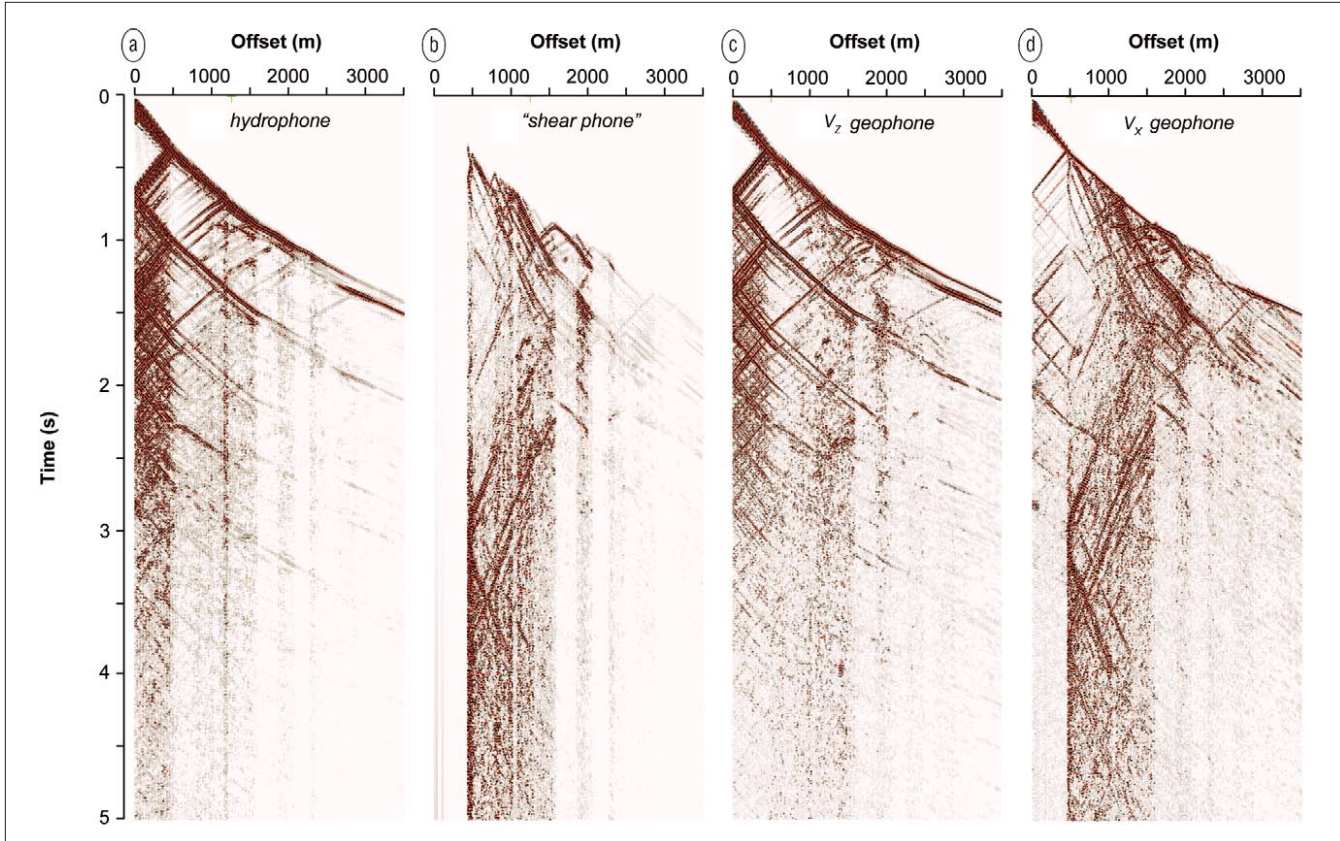


Figure 14. VSP for shot 412, (at 10 275 m, CDP 1645). Source to VSP offset is 25 m. Downgoing energy is dipping to the right side of the figures; upgoing energy is dipping to the left side. (a) Hydrophone records P-waves, (b) theoretical shear phone records S-waves, (c) vertical component geophone records both P-waves and S-waves, and (d) horizontal component geophones also records both P-waves and S-waves.

extension of the Marmousi model for use in the public and private domain by the geophysical research community at large. We created Marmousi2 with three goals in mind. First, we expect the synthetic data volume to provide a means for researchers, software vendors, service providers, and oil companies to evaluate, calibrate, and compare new developments in velocity analysis, seismic imaging, AVO, and impedance inversion. Second, we expect the numerical modeling community to use Marmousi2 as a basis for more complicated models that will include the effects of attenuation, anisotropy, complex stratigraphy, more sophisticated hydrocarbon fluid substitution formulae, and more innovative acquisition techniques. While of less interest to practicing geophysicists, our final objective is to provide a model that is large and complex enough for researchers to evaluate improvements in algorithm and computer architecture that will form the basis for truly 3D numerical modeling of a realistic seismic survey. The major limitation of Marmousi2 is that the data are 2D.

The Marmousi2 model and synthetic data have already been made available to many researchers throughout the world.

Suggested reading. "The Marmousi experience: Velocity model determination on a synthetic complex data set" by Versteeg (TLE, 1994). "Seismic amplitude interpretation" by Hilterman (SEG distinguished instructor short course, 2001). "Fourth-order finite-difference P-SV seismograms" by Levander (GEOPHYSICS, 1988). "Rock Physics—The link between rock properties and AVO response" by Castagna et al. (*Offset-dependent reflectivity – Theory and practice of AVO anomalies, Investigations in Geophysics no. 8*, SEG, 1993). "Absorbing boundary conditions for acoustic and elastic wave equations" by Clayton and

Engquist (*Numerical modeling of seismic wave propagation*, 13, SEG, 1990; reprinted from *Bulletin of the Seismological Society of America*, Volume 67:6, 1529-154). "Shear-wave velocity estimation in porous rocks: Theoretical formulation, preliminary verification and applications" by Greenburg and Castagna (*Geophysical Prospecting*, 1992). "The Marmousi2 model, elastic synthetic data, and an analysis of imaging and AVO in a structurally complex environment" by Martin (Master's dissertation, University of Houston, 2004), available from <http://www.agl.uh.edu/downloads/downloads.htm>. The reader can also download horizon files and associated model parameters, gridded velocity and density models, and images of seismic data and snapshots, as well as information on how to request digital copies of the synthetics. TLE

Acknowledgment: This work was made possible by the contributions of many colleagues and associates. First, we thank the Department of Energy for funding the "Next Generation Numerical Modeling" project led by Leigh House of Los Alamos National Laboratories. Next, we thank Shawn Larsen and Lawrence Livermore National Laboratories for providing us with an executable copy of the 3D finite-difference code, E3D, as part of this DOE project. The computation was performed at the University of Houston's Geoscience Center of Excellence provided by Sun Microsystems. We thank Don Larson at GX Technology for modifications necessary to GX-II to enable such a complicated model to be constructed. We also thank Aline Bourgeois at the IFP, and colleagues at Total and GX Technology. Finally, we thank Fred Hilterman for help in modifying the model to address an expanded suite of geologic problems and yet honor the original goals of the Marmousi experiment.

Corresponding author: gmartin@gxt.com